



# Chemomechanical weakening of muscovite quantified with in situ liquid nanoindentation

William M. Mook<sup>1,\*</sup> , Anastasia G. Ilgen<sup>2</sup>, Katherine L. Jungjohann<sup>3,4</sup>, and Frank W. DeIRio<sup>3</sup>

<sup>1</sup>Microsystems Engineering, Science and Applications Center, Sandia National Laboratories, Albuquerque, NM 87123, USA

<sup>2</sup>Climate Change Security Center, Sandia National Laboratories, Albuquerque, NM 87123, USA

<sup>3</sup>Material, Physical, and Chemical Sciences Center, Sandia National Laboratories, Albuquerque, NM 87123, USA

<sup>4</sup>Materials Science Center, National Renewable Energy Laboratory, Golden, CO 80401, USA

Received: 6 March 2022

Accepted: 6 May 2022

Published online:  
26 May 2022

© The Author(s) 2022

## ABSTRACT

Chemomechanical weakening of layered phyllosilicate muscovite mica was studied as a function of chemical environment via in situ liquid-nanoindentation under four conditions (dry, deionized water, and two NaCl solutions of different pH). While traditional indentation analyses of layered materials with extreme mechanical anisotropy have been limited due to displacement bursts (pop-ins), here the bursts were used as proxies for delamination, fracture, and spalling events. Since displacement bursts during an indent represent a stochastic process, 120 indents were conducted for each condition to generate statistically significant amounts of data. In total, over 9000 bursts were assessed using a load–displacement threshold criterion, classifying this as a high-throughput nanoscale fracture technique. For each burst, initiation load, initiation displacement, plastic zone volume at initiation, and energy dissipation were analyzed. A power-law relationship between the burst load and burst energy was noted which separated the bursts into two continuous distributions: (1) bursts due only to the mechanics of the indent and (2) bursts due to both the mechanics of the indent and the environment. By using a cumulative probability distribution, it was found that the NaCl solutions decreased the minimum plastic zone volume necessary to initiate a displacement burst by an order of magnitude relative to the dry condition. Finally, the underlying mechanisms explaining the trends in initiation volume as a function of environment were discussed, with a focus on the chemomechanical degradation processes via chemical attack and cation exchange.

Handling Editor: M. Grant Norton.

Address correspondence to E-mail: wmmook@sandia.gov

## Introduction

Chemical reactions at crack tips and on material surfaces can alter observed mechanical properties from the molecular- to continuum-scales. This recognition has led to new technologies, such as chemical–mechanical polishing [1] and hydraulic fracturing [2]. At the nano to microscales, chemical effects can define material degradation, and manifest as stress corrosion cracking [3] and liquid–metal embrittlement [4]. At the kilometer-scales, chemically assisted slow cracks drive the long-term consolidation processes, formation of fracture networks, and permeability changes in subsurface reservoirs [5, 6].

Chemical effects on fracture have been recognized for over a century [7, 8]. Rehbinder [8] showed that quartz and fluorite crystals fractured more easily in aqueous surfactant solutions. Similar to the Griffith criterion [7], Rehbinder suggested that surface adsorbates can decrease the work of formation for new surfaces during fracture, and therefore that the fracture toughness of a material can be dependent on the chemical environment [9]. Despite the maturity of this research field, current theoretical frameworks fail to predict how the energy release rate, crack growth rate, and geometry of subcritical cracks change with changing chemical environment and material properties. This is because there are a multitude of potential chemical mechanisms that can influence the effective fracture toughness, *e.g.*, adsorption reactions [8, 10–12], redox reactions [13], and chemical attack by a reactive species [14]. Anisotropy, characteristic of layered minerals and sedimentary rock formations, presents an additional challenge in predicting crack growth [15, 16]. Here, we focus on the chemical effects on fracture in the layered mineral muscovite—an abundant member from the mica group, and one of the primary components of rock formations.

The mica mineral group is important in subsurface engineering applications, including resource extraction, carbon sequestration, and nuclear waste storage, because it is susceptible to chemomechanical weakening due to its layered, anisotropic structure and has also been shown to control the strengths and mechanical anisotropies of laminated (layered) rocks such as shale due to its relative weakness in comparison to other silicates [17]. Moreover, mica group minerals are abundant, composing approximately 13% of the upper continental crust [18]. Muscovite is

in the dioctahedral subgroup of mica with an ideal chemical formula of  $\text{KAl}_2(\text{Si}_3\text{Al})\text{O}_{10}(\text{OH},\text{F})_2$  and is the most common of the 55 mica polytypes [19]. Muscovite is composed of TOT (tetrahedral–octahedral–tetrahedral) layered structures, where the ‘T’ layers are silicon oxide that sandwich the ‘O’ layer of aluminum oxide (Fig. 1, structure file from [20]). The ‘T’ layers have random substitutions of Al for Si, while the individual TOT structures are bonded together by potassium cations. TOT layers are nanometer-thick, crystalline sheets that facilitate easy basal slip and perfect basal cleavage on the (001) planes.

The layered structure of muscovite, as depicted in Fig. 1, leads to highly anisotropic mechanical behavior that is dictated by a number of deformation mechanisms depending on the crystallographic orientation of loading. Mares and Kronenberg [17] conducted uniaxial compression of macroscopic, single-crystal muscovite at 400 °C with a confining pressure of 200 MPa at a strain rate of  $10^{-5}$  and observed dislocation glide and low-angle kink boundary formation when loaded 45° to the (001) basal plane, kink band formation when loaded parallel to the basal plane, and fracture when loaded perpendicular to the basal plane. Additionally, the

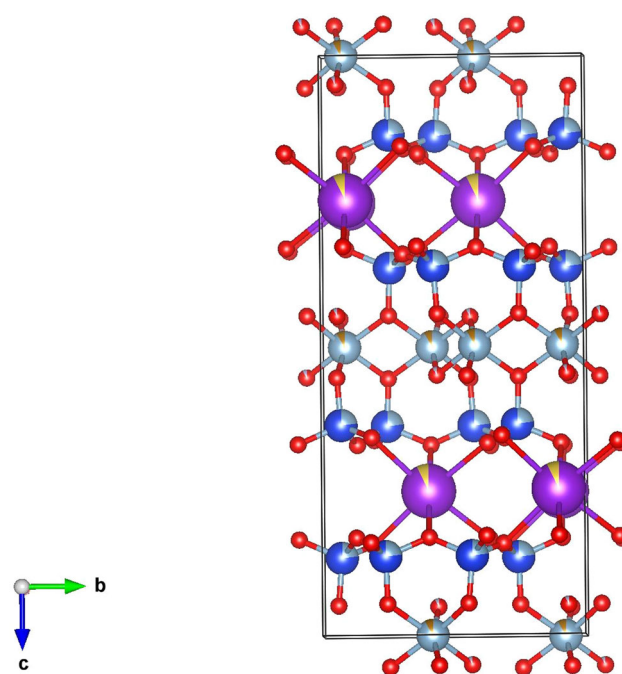


**Figure 1** Laminated structure of muscovite mineral visualized via the Vesta 3.3.9 software. Partial occupancies are due to isomorphous substitutions. Gray: Al, Red: O, Blue: Si, Purple: K, Yellow: Na.

authors found that muscovite could withstand an order of magnitude larger stresses when loaded perpendicular to the basal plane compared to 45° loading. However, despite the progress at the macroscale, microscale, and nanoscale testing of mica and other similarly layered materials has been limited due to this extreme anisotropy [21]. When conducting nanoindentation of mica, traditional analysis techniques are difficult to apply due to the large number of displacement bursts, also known as pop-ins, that occur. And while in situ liquid-nanoindentation was first conducted over 20 years ago [22], it has not been widely employed to analyze this material system due to the difficulties in quantifying results.

In this paper, in situ liquid nanoindentation was used to study the chemomechanical weakening of muscovite, with displacement bursts used as a proxy for kinking, delamination, fracture, and spalling events. Four environmental conditions were explored: (1) dry, (2) deionized (DI) water, (3) 0.1 M NaCl aqueous solution (pH 9.8), and (4) 0.1 M NaCl aqueous solution (pH 12.0). For each load  $P$ -displacement  $h$  trace, the reduced modulus  $E_r$  and hardness  $H$  were evaluated using the Oliver–Pharr method [23, 24]; changes to  $E_r$  and  $H$  were explained through changes in the displacement burst distributions and mica stiffness. For each displacement burst, the initiation displacement  $h_b$ , initiation load  $P_b$ , plastic zone volume at initiation  $V_{pl}$ , and energy dissipation  $E_b$  were assessed using a  $d(P)/d(h) = 0.3 \mu\text{N}/\text{nm}$  metric. A power-law relation between the burst load and energy was noted which separated the bursts into two continuous distributions: (1) bursts due only to the mechanics of the indent and (2) bursts due to both the mechanics of the indent and the environment. Finally, the plastic zone volumes  $V_{pl}$  necessary to initiate a burst were calculated assuming a hemispherical region under the tip; decreases in the minimum volume necessary for a displacement burst as a function of environment were justified through chemical attack of hydroxyl ion  $\text{OH}^-$  on Si—O bonds and ion exchange of  $\text{K}^+$  for  $\text{Na}^+$  at the surface defect sites. The mechanistic underpinnings of the property changes were then explored, with a focus on the consequences of environmental corrections to the fracture properties and power-law scaling in the energy data.

## Experimental methods

High-quality synthetic muscovite mica (V1) was purchased from MTI Corporation with lateral dimensions of  $1.5 \text{ cm}^2$  and a thickness of  $270 \mu\text{m}$ . The muscovite mica was adhered to the bottom of a petri dish via Loctite 409 Superbonder epoxy from Henkel, such that the epoxy was completely contained under the sample. Four environmental conditions were explored: (1) dry, (2) DI water, (3) 0.1 M NaCl aqueous solution (pH 9.8) and (4) 0.1 M NaCl aqueous solution (pH 12.0). The pH values were chosen because the silicate framework is susceptible to chemical attack by hydroxyl ions ( $\text{OH}^-$ ) [14]. The measured dissolution rates for muscovite are on the order of  $1.20 \times 10^{-16} \text{ mol cm}^{-2} \text{ s}^{-1}$  at pH 9.5– $4.45 \times 10^{-16} \text{ mol cm}^{-2} \text{ s}^{-1}$  at pH 11.8 and at  $70 \text{ }^\circ\text{C}$  [25]. A new crystal was used for each of the three liquid conditions. The samples were stored in an  $\text{N}_2$  box and nanoindentation was conducted within 12 h after removal from the box.

Nanoindentation was performed on a Hysitron TriboIndenter 900 with an in situ liquid Berkovich-geometry indenter tip. Prior to nanoindentation, the tip area function and load frame compliance were calibrated over the entire load range of the instrument using fused silica as the reference material. For the Berkovich tip, the tip area function  $A(h)$  was defined as

$$A(h_c) = C_0h^2 + C_1h^1 + C_2h^{1/2} + C_3h^{1/4} + C_4h^{1/8} + C_5h^{1/16} \quad (1)$$

where  $h$  is the contact depth and  $C_0$  through  $C_5$  are coefficients related to tip shape. Assuming a reduced modulus  $E_r = 69.6 \text{ GPa}$  for fused silica,  $C_0$ – $C_5$  were found through fits to the calibration data. Following calibration, the measurements on muscovite consisted of loading to a maximum load of 10 mN at an indentation strain rate of 0.1 [26], with a 5 s hold at maximum load followed by a 5 s unload. For dry nanoindentation, the relative humidity in the laboratory never exceeded 30%. A total of 120 indents (three  $5 \times 8$  grids) were conducted, with each grid point spaced  $60 \mu\text{m}$  apart. For nanoindentation in DI water and NaCl aqueous solutions, approximately 25 mL of liquid was dispensed into the 9 cm diameter petri dish in order to completely cover the sample to a depth of approximately 3.5 mm. The tip was brought into contact with the sample and retracted  $50 \mu\text{m}$  so that 99% of the shaft was submerged in the

liquid as it would be during indentation. Since the liquid affects the perceived load on the tip and the amount of force necessary to move the tip in the  $z$ -axis [27], the  $z$ -axis calibration was completed in the liquid. At this point, the liquid nanoindentation method was identical to the standard, dry indentation process. All indentation arrays were centered 4 mm away from the edge of the sample and were completed within 12 h after the muscovite was immersed in the liquid. While each condition was indented 120 times, several indents did not run as planned due to an inability to locate the surface. Therefore, the number of indents analyzed for each condition were 115 for dry, 119 for DI water, 118 for NaCl (pH 9.8), and 117 for NaCl (pH 12.0). For lower load (2 mN) indents, subsequent scanning probe microscopy (SPM) images were captured at a normal force of 2  $\mu\text{N}$  and a scan rate of 5  $\mu\text{m/s}$ .

$E_r$  and  $H$  were assessed using the Oliver–Pharr method [23, 24], with the caveat that displacement bursts introduced scatter and uncertainty in the calculated values. The method assumes that the initial point of unloading is purely elastic. Therefore, the initial slope of the load–displacement data is the elastic stiffness  $S$  as given by

$$S = \beta \frac{2}{\sqrt{\pi}} E_r \sqrt{A} \quad (2)$$

where  $\beta$  is a dimensionless parameter determined by tip geometry ( $\beta = 1.034$  for a Berkovich tip).  $E_r$  is given by

$$\frac{1}{E_r} = \frac{1 - \nu_1^2}{E_1} + \frac{1 - \nu_2^2}{E_2} \quad (3)$$

where  $E_1$  and  $E_2$  are the Young's moduli of the tip and substrate and  $\nu_1$  and  $\nu_2$  are the Poisson's ratios of the tip and substrate.  $H$ , which can also be considered the average contact stress  $\bar{\sigma}_c$ , is defined by

$$H = \bar{\sigma}_c = \frac{P_{\max}}{A} \quad (4)$$

where  $P_{\max}$  is the maximum load. The individual displacement bursts were also studied to assess (1) load and displacement at initiation, (2) energy dissipated, and (3) plastic zone volume. For this work, an individual burst was identified through an abrupt increase in the derivative of the load–displacement data to a value above  $d(P)/d(h) = 0.3 \mu\text{N/nm}$ . Once all displacement bursts were identified via this metric, the initiation load, initiation displacement, and

total displacement for each burst were evaluated. It was then straightforward to calculate the energy expended in each burst  $E_b$  via the area under the load–displacement curve during the burst. Finally, it was necessary to estimate the plastic zone volume at initiation  $V_{\text{pl}}$  for each burst, as this was used as a metric to gauge the influence of liquid on burst generation. To resolve  $V_{\text{pl}}$ , a hemispherical volume centered under the tip was assumed, such that

$$V_{\text{pl}} = \frac{4}{3} \pi R_{\text{pl}}^3 \quad (5)$$

where  $R_{\text{pl}}$  is the plastic zone radius.  $R_{\text{pl}}$  was estimated using the analytical expression developed by Chen and Bull [28],

$$R_{\text{pl}} = h_b \left( -12.907 \left[ \frac{H}{E_r} \right] + 4.5451 \right) \quad (6)$$

where  $h_b$  is the depth of the indentation tip at the initiation of a burst and the  $H/E_r$  values are taken from the Oliver–Pharr analysis.

## Results

### Reduced modulus and hardness

Indentation of a layered material such as mica is dominated by displacement bursts to the extent that it is difficult to reproduce a specific load–displacement response. This can be seen in Fig. 2a through d. Figure 2a shows 115 indents into the dry (001) muscovite surface. Visual inspection of Fig. 2a shows that the majority of individual indents experience at least one large displacement burst at loads  $< 5$  mN. Inspection of all indents in Fig. 2b through d showed that the response of mica in liquid produced displacement bursts at lower loads and displacements when compared to the dry case. The majority of indents demonstrated large displacement bursts at  $< 3$  mN during indentation in DI water,  $< 1.9$  mN during indentation in the 0.1 M NaCl pH 9.8 aqueous solution, and  $< 1.3$  mN in the 0.1 M NaCl pH 12.0 aqueous solution. This data have been decomposed into burst-only data (Fig. 2e through h) and burst-free data (Fig. 2i through l). The burst-free data collapses to a relatively repeatable load–displacement response for each environmental condition. The influence of the liquid can be observed qualitatively in Fig. 2b through d which shows the  $P$ – $h$  response of

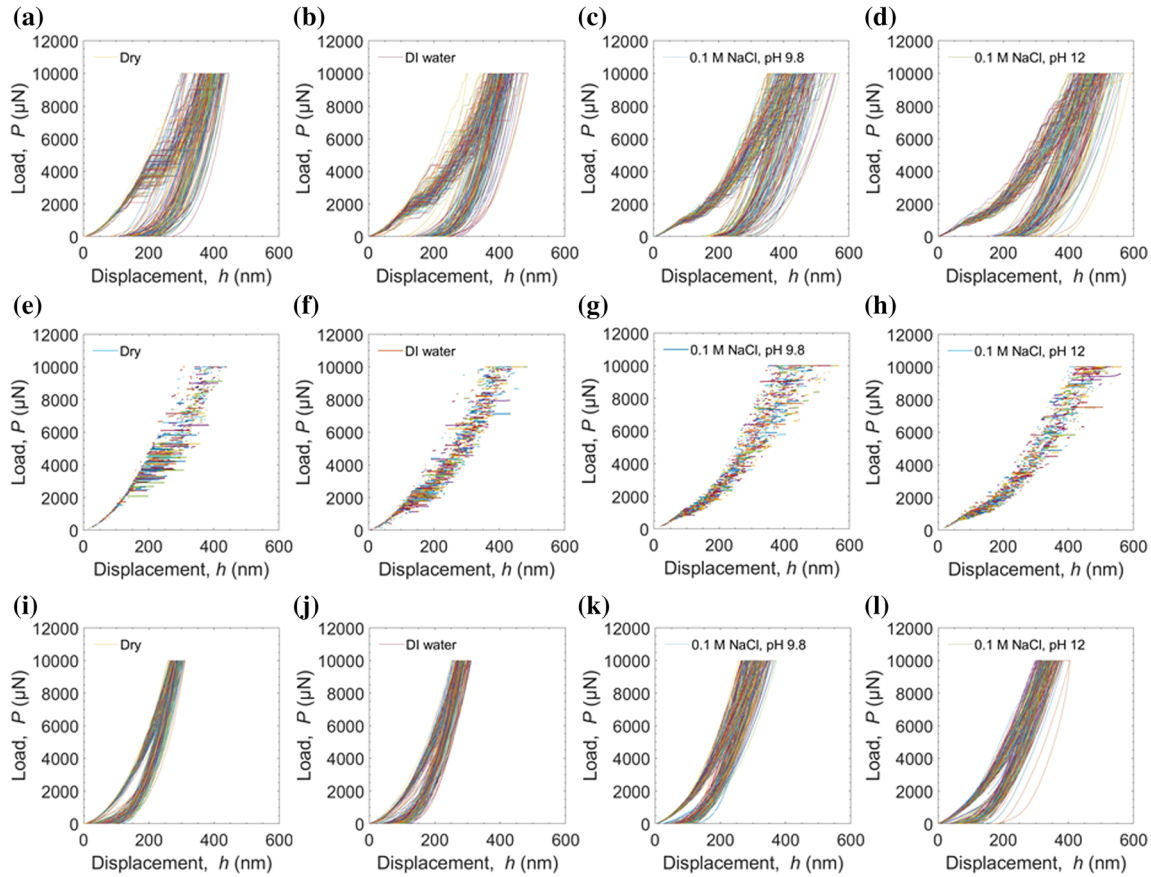


**Figure 2** Original load–displacement,  $P$ – $h$  response for **a** dry (115 indents), **b** DI water (119 indents), **c** 0.1 M NaCl pH 9.8 (118 indents) and **d** 0.1 M NaCl pH 12.0 (117 indents). This data have been decomposed into burst-only data (**e–h**) and burst-free data (**i–l**). The burst-free data collapses to a relatively repeatable load–displacement response for each environmental condition. Figure 2b through d also suggests that both  $E_r$  (the initial elastic unloading slope) and  $H$  (10 mN load divided by a larger contact area) decrease during indentation in liquid.

The reduced modulus and hardness of each indent was calculated using Eqs. (2–4), and the resulting means and standard deviations for each environmental condition are summarized in Table 1. From the table, it is clear that  $E_r$  and  $H$  decreased in the following order: dry, DI water, 0.1 M NaCl pH 9.8, and 0.1 M NaCl pH 12. The reduced modulus and hardness decreased by over 40% when comparing 0.1 M NaCl pH 12 to dry indentation. This was mainly due to an increase in frequency of displacement bursts for muscovite in liquid and a decrease of the muscovite stiffness due to intercalation of the liquid between the sheets once surface fractures occurred. Interestingly,  $E_r$  and  $H$  decreased at a

displacement response for each environmental condition. Whether comparing the data with or without the bursts, the environment affects both the maximum indentation depth (decreasing hardness) and initial slope of the unloading curve (decreasing indentation modulus).

**Table 1** Reduced modulus  $E_r$  and hardness  $H$  values (means and standard deviations) for each of the four environmental conditions

Condition	$E_r$ (GPa)	$H$ (GPa)	$H/E_r$
Dry	$55.1 \pm 5.8$	$3.53 \pm 0.77$	0.064
DI water	$52.8 \pm 6.5$	$3.12 \pm 0.51$	0.061
0.1 M NaCl pH 9.8	$39.9 \pm 9.7$	$2.27 \pm 0.47$	0.058
0.1 M NaCl pH 12	$31.0 \pm 8.7$	$2.05 \pm 0.48$	0.066

$E_r$  and  $H$  decreased in the following order: dry, DI water, 0.1 M NaCl pH 9.8, and 0.1 M NaCl pH 12.  $H/E_r$  remained relatively constant at  $0.062 \pm 0.004$

constant ratio, such that  $H/E_r$  remained relatively constant at  $0.062 \pm 0.004$ .

### Energy dissipation

The energy dissipated by an individual displacement burst can be calculated as the area under the load–

displacement curve from the beginning to the end of the displacement burst, in other words the burst length multiplied by its corresponding load generally produces an energy on the order of pJ ( $J = N \cdot m$ ). In order to address which deformation modes the displacement bursts represent, it was necessary to analyze indents that generate only one or two displacement bursts. Figure 3a depicts three shallow indents with a maximum load of 2 mN. Subsequent scanning probe microscopy (SPM) imaging of each indent revealed that unique deformation modes were responsible for each of the displacement bursts. The SPM image of the indent in Fig. 3b indicated delamination between the muscovite basal layers labeled B1, which produced a step-height of  $\approx 1.6$  nm as shown by the difference in the green and red markers on the associated line scan;  $h_b$ ,  $P_b$ , and  $E_b$  for this displacement burst were found to be 67.3 nm, 576  $\mu\text{N}$ , and 2.1 pJ, respectively, as shown in Table 2. The SPM image of the indent in Fig. 3c showed radial fracture originating at the contact point between the sample and the apex of the indenter tip, where the two major bursts labeled C1 and C2 expended 7.7 pJ and 11.2 pJ, respectively. Event C2 occurred on unloading; crack growth in low-toughness materials during unloading of an indentation is common [29]. The SPM image of the indent in Fig. 3d showed spalling of the muscovite to a depth of 35 nm, where the two major bursts labeled D1 and D2 (D2 occurred during the hold period) expended 12.3 pJ and 20.8 pJ, respectively. In this latter case, the line scan shows

**Table 2** Initiation displacement  $h_b$ , initiation load  $P_b$ , and energy dissipation  $E_b$  for the primary displacement bursts in Fig. 3

Burst	$h_b$ (nm)	$P_b$ (mN)	$E_b$ (pJ)	Deformation mode
B1	67.3	576	2.1	Delamination
C1	160.1	1884	7.7	Fracture
C2	150.4	1477	11.2	Fracture
D1	98.6	951	12.3	Fracture/spall
D2	185.6	1998	20.8	Fracture/spall

A burst energy of 2.1 pJ was linked to interlayer delamination, while fracture occurred at energies greater than 7 pJ

that the base of the spalled material lies along a single basal layer, indicating that the base was formed through a delamination event. In all, the results in Table 2 are in agreement with prior work that suggested smaller displacement bursts represent delamination [30] or kinking of the mica layers [31, 32], whereas larger bursts represent fracture or spallation [30, 33].

Displacement bursts during mechanical deformation are a stochastic process [34–36]. Therefore, large numbers of bursts were necessary to generate enough statistics in order to properly characterize them. Muscovite in the dry condition was indented 115 times generating a total of 1467 displacement bursts for an average of 12.8 bursts per indent. The same sample was submerged in DI water and indented 119 times causing a total of 2178 displacement bursts for an average of 18.3 bursts per indent. A second

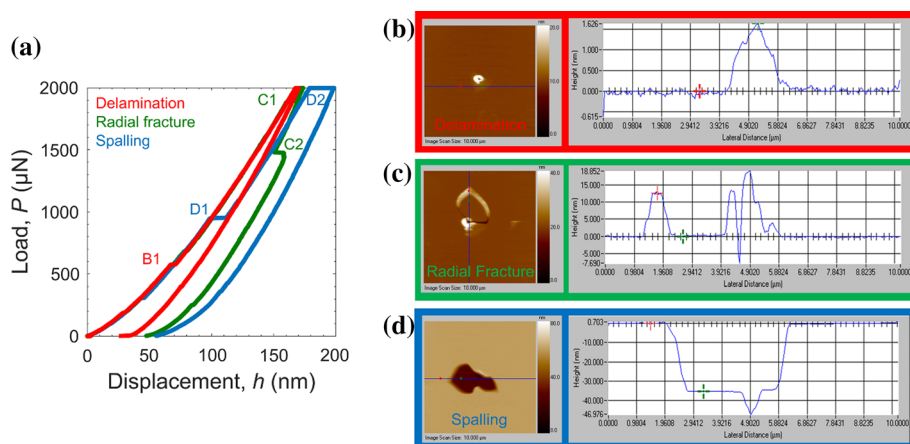


**Figure 3** a Nanoindentation of mica to a maximum load of 2 mN. Each indent exhibits at least one displacement burst, and the five major bursts are also detailed in Table 2. b–d Subsequent SPM imaging of each indent revealed a unique deformation mode. b The red indent indicated delamination between the muscovite

basal layers labeled B1 and a step-height of 1.6 nm. c The green indent showed radial fracture originating at the contact point and two major bursts labeled C1 and C2. d The blue indent showed spalling and two major bursts labeled D1 and D2.

muscovite sample submerged in a 0.1 M NaCl solution with a pH of 9.8 was indented 118 times that produced 2844 bursts (average of 24.1 bursts per indent), and a third sample submerged in a 0.1 M NaCl solution with a pH of 12.0 was indented 117 times generating 2942 bursts (average of 25.1 bursts per indent). Analysis of all conditions totaled 469 indents accounting for 9431 displacement bursts; displacement bursts during unloading were not considered in this analysis. The energy expended during each displacement burst was then calculated using the area under the  $P$ – $h$  curve. Figure 4(a–d) summarizes the resulting  $E_b$  as a function of  $P_b$  data for all four conditions on log–log plots. From the data, a clear trend was observed that follows a power-law relationship of

$$E_b = 4.5 \times 10^{-5} P_b^{1.6} \tag{7}$$

This power-law expression was used to separate the displacement bursts into two groups. Bursts falling below the curve are graphed in black, while bursts falling above the curve are graphed in red. Figure 4e–h shows the bursts graphed as a function of indentation load and displacement in order to give context to the energy-load plots.

Histograms of the energy expended for the displacement burst subsets both above and below the power-law expression are presented in Fig. 5. In

order to determine if they are generated from the same or different continuous distributions, the burst subsets were analyzed using a two-sample Kolmogorov–Smirnov test [37]. A comparison matrix of the asymptotic  $p$ -values from the test is shown in Table 3, where italic indicates that the null hypothesis was not rejected ( $p$  value > 0.05, such that the two histograms are assumed to come from the same distribution), while bold indicates that the null hypothesis was rejected ( $p$  value < 0.05, such that the histograms are assumed to come from different distributions). As shown in Table 3, histograms of the bursts below the power-law relationship are from the same distribution for each of the four conditions. This implies bursts below Eq. (7) are independent of the environment, and only depend on the mechanics of the indent. In other words, this subset of displacement bursts must be spatially isolated from the environment and occur deep within the plastic zone of the indent. In contrast, displacement bursts above Eq. (7) come from different distributions, showing that environment does play a role in the generation of these events. This subset of bursts was exposed to the environment, be it air or liquid. The bursts were generated by a combination of both the mechanics of the indent and the environment. Equation 7 is therefore physically meaningful even though it is empirical. For bursts above the power law, liquid

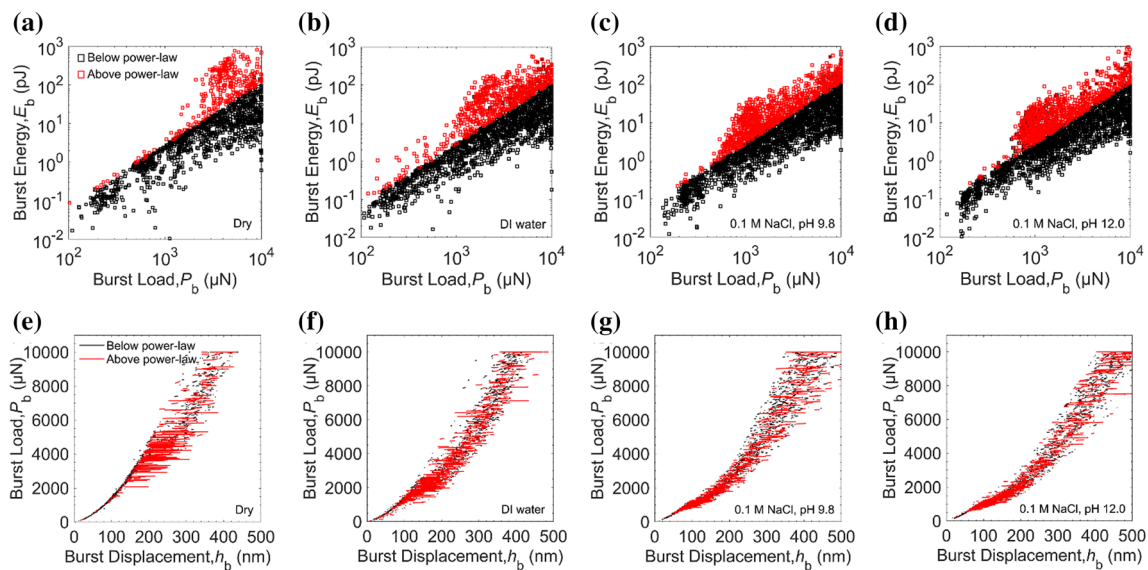


**Figure 4** a–d  $E_b$  as a function of  $P_b$  for a dry, b DI water, c 0.1 M NaCl pH 9.8 and d 0.1 M NaCl pH 12.0. The power-law relationship separates the environmental (red) from the mechanical (black) contributions to fracture. e–h  $P_b$  as a function of  $h_b$  for

e dry, f DI water, g 0.1 M NaCl pH 9.8 and h 0.1 M NaCl pH 12.0. In every case, the red bursts are exposed to the environment, while the black bursts are spatially isolated from the environment.

**Figure 5**  $E_b$  histograms showing displacement burst distributions below and above the power law relationship. **a–c** Below the power law, the liquids generate more bursts, but from the same continuous distribution. **d–f** Above the power law, indentation in liquid constantly generates higher burst counts with energies in the 1–100 pJ range.

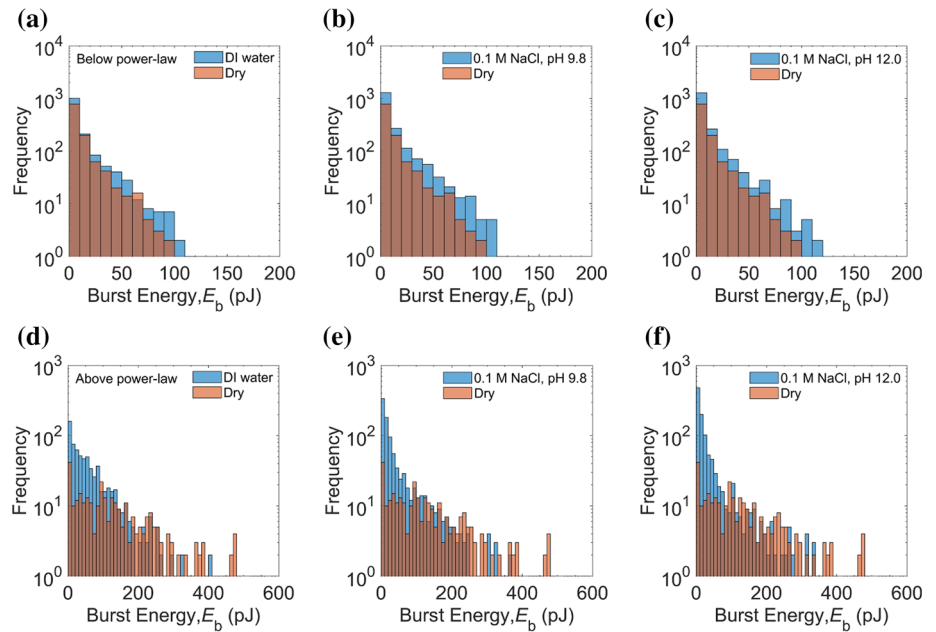


**Table 3** Comparison matrix of asymptotic  $p$  values from the two-sample Kolmogorov–Smirnov test, where the bottom-left section compares  $E_b$  distributions from below the power law ( $p$  value  $> 0.05$ ,

same distribution) and the top-right section compares distributions from above the power law ( $p$  value  $< 0.05$ , different distributions)

Condition	Dry	DI water	0.1 M NaCl pH 9.8	0.1 M NaCl pH 12
Dry	–	$1.6 \times 10^{-25}$	$9.2 \times 10^{-46}$	$3.2 \times 10^{-60}$
DI water	0.357	–	$5.6 \times 10^{-21}$	$9.9 \times 10^{-37}$
0.1 M NaCl pH 9.8	0.206	0.682	–	$4.8 \times 10^{-9}$
0.1 M NaCl pH 12	0.083	0.064	0.133	–

increases the likelihood of bursts with  $E_b$  in the range of 1–100 pJ when compared to the dry condition. As a point of reference, an  $E_b$  of 2.1 pJ was associated with interlayer delamination, while fracture occurred at  $E_b$  greater than 7 pJ, as shown in Table 2.

### Plastic zone volume

The plastic zone volume  $V_{pl}$  for each displacement burst was calculated with Eqs. (5) and (6), using the  $h_b$  values for each burst and the  $H/E_r$  ratios in Table 1. The burst energy as a function of plastic zone volume for all bursts is shown in Fig. 6a. To reduce data, the first displacement burst for each indent with an energy  $E_b$  greater than the specified value was identified. The volume  $V_{pl}$  for that burst was tabulated for each indent to produce a cumulative distribution function (CDF) for each condition. As an example, the CDF for the first burst from each indent with an expended energy above 5 pJ is shown both

for bursts below the power law in Fig. 6b, and for bursts above the power law in Fig. 6c. This was repeated for each condition over an energy range from 0.1 to 100 pJ in 0.1 pJ increments.

The mean value of the plastic zone volume of each CDF is graphed as a function of displacement burst energy in Fig. 7, with the displacement bursts below the power law in Fig. 7a and the displacement bursts above the power law in Fig. 7b. Figure 7b shows that the minimum threshold volumes for environmentally assisted fracture decreased with the addition of liquid. In more detail, the threshold volumes for dry muscovite, DI water, and the two 0.1 M NaCl solutions were  $0.45 \mu\text{m}^3$ ,  $0.15 \mu\text{m}^3$ , and  $0.04 \mu\text{m}^3$ , respectively. Thus, the NaCl solutions decreased the minimum volume for environmentally assisted fracture by an order of magnitude compared to dry mica. For all cases, bursts with volumes below these threshold values were due entirely to the mechanics



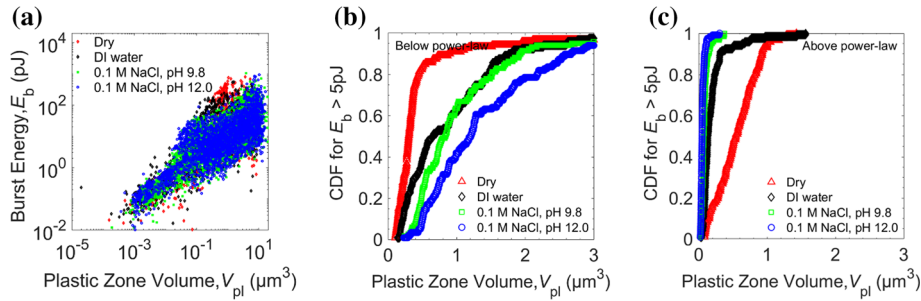


**Figure 6** **a**  $E_b$  as a function of  $V_{pl}$  for all displacement bursts. **b–c** The first displacement burst for each indent with an  $E_b$  greater than 5 pJ was graphed as a CDF for bursts **b** below the power-law relationship and **c** above the power-law relationship.

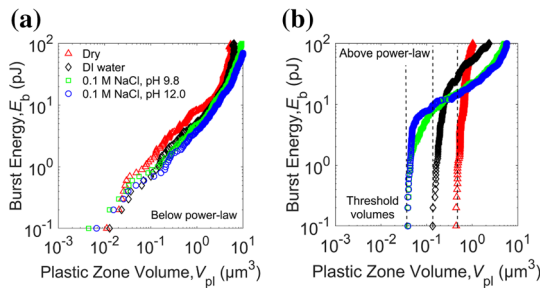


**Figure 7**  $E_b$  as a function of  $V_{pl}$  for bursts **a** below the power-law relationship and **b** above the power-law relationship. In **a**, the fracture events occurred internally and were not exposed to the environment. In **b**, fracture events were exposed to the environment via fractures that intersected with the sample surface. The threshold volumes for dry mica, DI water, and the two 0.1 M NaCl solutions were  $0.45 \mu\text{m}^3$ ,  $0.15 \mu\text{m}^3$ , and  $0.04 \mu\text{m}^3$ , respectively.

of indentation and were not influenced by the environment. These initial events can be seen in Fig. 7a below the environmental threshold  $V_{pl}$  for each condition. For confirmation, see the similarity in deformation response for loads below 1 mN in Fig. 2b and Fig. 4e–h. These bursts depicted the first kinking and delamination events and were internal to the structure. However, once surface fractures and spalling occurred, liquid intercalated between the mica layers, producing bursts from both environmental assistance and indentation mechanics.

### Discussion

Two points from the earlier results required further examination: (1) the presence of mechanically dominated and environmentally assisted  $E_b$  distributions and (2) the decrease in the minimum  $V_{pl}$  for environmentally assisted fracture by an order of

magnitude relative to dry mica. On point (1), the fracture bursts generated by “sharp” indenter tips are governed by the underlying elastic–plastic stress fields, and as such, are found to involve the hardness-to-modulus ( $H/E$ ) ratio and fracture toughness [38]. For a material in an inert environment, it was illustrated that the length of an indentation crack  $c_0$  in an unrelaxed residual stress field is given by [39]

$$c_0 = \left(\frac{\chi_0}{T_0}\right)^{2/3} P^{2/3} \tag{8}$$

where  $T_0$  is the toughness and  $\chi_0$  is a dimensionless factor based on the geometries of subsurface cracks and stress fields (both in inert conditions). In previous work, the dimensionless factor was found to be  $\chi_0 = 0.016(H/E)^{-1/2}$ ; the initial term in this empirical relationship was determined by averaging data for “well-behaved” ceramic materials [39]. For a material in air or liquid, it was later shown that the length of an indentation crack  $c_{env}$  in a relaxed residual stress field is given by [40]

$$c_{env} = \left(\frac{\chi_{env}}{T_{env}}\right)^{2/3} P^{2/3} \tag{9}$$

where  $T_{env}$  is the toughness and  $\chi_{env}$  is the dimensionless factor in environmental conditions. The effects of the environmental conditions on the geometries of subsurface cracks and stress fields can be quantified by combining Eqs. (8) and (9) to yield [40]

$$c_{env} = \left(\frac{\chi_0 - \Delta\chi_{env}}{T_0 - \Delta T_{env}}\right)^{2/3} P^{2/3} \tag{10}$$

where  $\Delta\chi_{env} = \chi_0 - \chi_{env}$  and  $\Delta T_{env} = T_0 - T_{env}$  are environmental corrections that are both positive. Previous data on a range of ceramics via inert [41] and reactive [42] indentation strength measurements

suggest that  $\Delta\chi_{\text{env}} \approx 0.2\chi_0$  and  $\Delta T_{\text{env}} \approx 0.5T_0$ , consistent with observations [39] that show  $c_{\text{env}} \approx 2c_0$  [40]. However, the exact details of the  $c_{\text{env}}/c_0$  ratio are known to be dependent on test conditions (e.g., indentation load [43] and moisture content [44]). Despite the dependencies, it is clear that the differences in the overall  $E_b$  distributions (Fig. 4) were from changes in the environmental conditions ( $\Delta\chi_{\text{env}}$  and  $\Delta T_{\text{env}}$ ), and not due to deviations in the inert fracture properties ( $\chi_0$  and  $T_0$ , where  $\chi_0 \sim (H/E)^{-1/2}$  and  $H/E$  is constant for all conditions). This idea is further supported by Fig. 5 and Table 3, where the  $E_b$  distributions below Eq. (7) are statistically similar (and governed by the mechanics of the indent) and the  $E_b$  distributions above Eq. (7) are statistically different (and dictated by the mechanics of the indent and the environment).

On point (2), the two NaCl solutions exhibited the same threshold volumes for environmentally assisted fracture, but different fracture efficiencies for energies ranging from  $1.5 \text{ pJ} < E_b < 14 \text{ pJ}$ ; the pH 12 solution was more efficient in producing bursts in that range. This is due to the increase in pH, or activity of the hydroxyl ions ( $\text{OH}^-$ ). This increase in efficiency can be explained with two plausible chemical mechanisms: chemical attack by the hydroxyl ions on the Si–O bonds (like that for quartz) [14] and ion exchange, where  $\text{Na}^+$  in solution replaces  $\text{K}^+$  in muscovite at the frayed surface edges and possibly within surface defect sites, inducing lattice strain due to size mismatch [45]. For burst energies from  $14 \text{ pJ} < E_b < 50 \text{ pJ}$ , muscovite submerged in DI water had the smallest average plastic zone size, while dry muscovite had the smallest plastic zone size for energies  $> 50 \text{ pJ}$ . The large number of bursts generated by the liquid environment decreased the stored elastic energy in the plastic zone to a level that made it difficult for the average contact stress to build to a high enough value to generate large bursts. This is similar to plate tectonics, as it is difficult for an active fault with numerous small earthquakes to store up enough energy to produce a catastrophic earthquake, whereas a less-active fault can fail catastrophically [46]. Interestingly, earthquakes are a standard example of a self-organized critical (SOC) system, a dynamic system that organizes itself to a critical point irrespective of the initial state [47, 48]. At this critical point, a model SOC system exhibits power-law scaling of event sizes, event durations, and in some cases, the  $1/f$  scaling of the power

spectra [49]. As such, the self-similar or scale-free behavior is described via a scaling exponent  $\alpha$ , enabling features at one scale to depict features at another scale across two or more orders of magnitude. Several small-scale mechanical phenomena demonstrate SOC behavior, including microfracture in disordered materials [50], shear-induced rearrangements in two-dimensional foams [51], dislocation motion in Ni [35] and Cu microcrystals [52], and structural transitions in self-assembled monolayers [53]. Two common themes were clear from these systems: the extracted values for  $\alpha$  (1.3–1.8) were in agreement with those from theoretical models (1.2–2.0) [54] and the subsequent scaling behavior was used to link the nanoscale events to macroscale phenomena. Curiously, the power-law trends detected in Fig. 4 ( $\alpha = 1.6$ ) and Fig. 5 ( $\alpha = 1.2$ , trendline not shown) fell within these ranges, signifying that chemomechanical weakening of muscovite *could* represent an SOC system. If so, the bursts in liquid nanoindentation can potentially be used as proxies for delamination, fracture, and spalling events in macroscale layered rocks such as shale, making this new approach a useful tool the development of effective subsurface engineering strategies.

## Conclusions

In summary, in situ liquid nanoindentation was used to characterize chemomechanical weakening of muscovite in four different environmental conditions. From the  $P$ – $h$  traces, it was found that  $E_r$  and  $H$  decreased by over 40% when comparing 0.1 M NaCl pH 12 to dry indentation, mainly due to an increase in frequency of displacement bursts and a decrease of the mica stiffness. However,  $E_r$  and  $H$  decreased at a constant ratio, such that  $H/E_r$  remained invariant with environment. The  $P$ – $h$  traces also demonstrated a large number of displacement bursts. Subsequent SPM imaging of selected low-load indents revealed that bursts were linked to unique deformation modes (e.g., delamination, radial fracture, and spalling) at  $E_b$  from 2.1 to 20.8 pJ. The  $E_b$  data from all bursts exhibited a power-law trendline as a function of  $P_b$ ; bursts below the trendline originated from a continuous  $E_b$  distribution and were dictated solely by the mechanics of the indent, whereas bursts above the trendline came from disparate  $E_b$  continuous distributions and were controlled by both mechanics and

environment. The minimum  $V_{pl}$  for environmentally assisted fracture decreased by an order of magnitude for the NaCl solutions relative to the dry case. Moreover, an increase in pH led to an increase in fracture efficiency in the low  $E_b$  regime, presumably due to an increase in  $\text{OH}^-$  chemical activity and attack by the hydroxyl ions on the silicate framework and, potentially, an increase in lattice strain at the frayed surface edges and within surface defect sites due to  $\text{K}^+$  for  $\text{Na}^+$  cation exchange. Future work will look to quantify the environmental corrections to fracture ( $\Delta\chi_{env}$  and  $\Delta T_{env}$ ) using measurements in inert conditions and to explore the possibility of scale-free behavior through a mean-field theory model.

## Acknowledgements

This research was funded by Sandia National Laboratories Laboratory Directed Research and Development (LDRD) program. Data collection and initial interpretation were funded by LDRD #192762; data analysis and manuscript preparation were funded by LDRD #222398. This work was performed, in part, at the Center for Integrated Nanotechnologies (CINT), an Office of Science User Facility operated for the U.S. Department of Energy (DOE) Office of Science. Sandia National Laboratories is a multimission laboratory managed and operated by National Technology & Engineering Solutions of Sandia, LLC, a wholly owned subsidiary of Honeywell International Inc., for the U.S. Department of Energy's National Nuclear Security Administration under contract DE-NA0003525. This paper describes objective technical results and analysis. Any subjective views or opinions that might be expressed in the paper do not necessarily represent the views of the U.S. Department of Energy or the United States Government. The authors declare that they have no conflict of interest.

**Open Access** This article is licensed under a Creative Commons Attribution 4.0 International License, which permits use, sharing, adaptation, distribution and reproduction in any medium or format, as long as you give appropriate credit to the original author(s) and the source, provide a link to the Creative Commons licence, and indicate if changes were made. The images or other third party material in this article are included in the article's Creative Commons

licence, unless indicated otherwise in a credit line to the material. If material is not included in the article's Creative Commons licence and your intended use is not permitted by statutory regulation or exceeds the permitted use, you will need to obtain permission directly from the copyright holder. To view a copy of this licence, visit <http://creativecommons.org/licenses/by/4.0/>.

## References

- [1] Jiang M, Wood NO, Komanduri R (1998) On chemo-mechanical polishing (CMP) of silicon nitride ( $\text{Si}_3\text{N}_4$ ) work material with various abrasives. *Wear* 220:59–71
- [2] Osiptsov AA (2017) Fluid mechanics of hydraulic fracturing: a review. *J Petrol Sci Eng* 156:513–535
- [3] Dunning JD, Lewis WL, Dunn DE (1980) Chemomechanical weakening in the presence of surfactants. *J Geophys Res* 85:5344–5354
- [4] Westwood ARC (1974) Tewksbury lecture: control and application of environment-sensitive fracture processes. *J Mater Sci* 9:1871–1895. <https://doi.org/10.1007/BF00541760>
- [5] Atkinson BK, Meredith PG (1987) The theory of subcritical crack growth with applications to minerals and rocks. In: Atkinson BK (ed) *Fracture mechanics of rock*. Elsevier, Amsterdam, pp 111–164
- [6] Dunning J, Douglas B, Miller M, McDonald S (1994) The role of the chemical environment in frictional deformation: stress corrosion cracking and comminution. *Pageophysics* 143:151–178
- [7] Griffith AA (1921) The phenomena of rupture and flow in solids. *Philos Trans R Soc A* 221:163–198
- [8] Rehbinder PA (1928) VI Congress of Russian Physicists. OGIZ, Moscow, p 29
- [9] Westwood ARC, Ahearn JS, Mills JJ (1981) Developments in the theory and application of chemomechanical effects. *Colloids Surf* 2:1–35
- [10] Malkin AI (2012) Regularities and mechanisms of the Rehbinder's effect. *Colloid J* 74:223–238
- [11] Ilgen AG, Mook W, Tigges AB, Choens RC, Artyushkova K (2018) Chemical controls on the propagation rate of fracture in calcite. *Sci Rep* 8:164656
- [12] Choens RC, Wilson J, Ilgen AG (2021) Strengthening of calcite assemblages through chemical complexation reactions. *Geophys Res Lett* 48:e2021GL094316
- [13] Gleizer A, Peralta G, Kermode JR, De Vita A, Sherman D (2014) Dissociative chemisorption of  $\text{O}_2$  inducing stress

- corrosion cracking in silicon crystals. *Phys Rev Lett* 112:115501
- [14] Dove PM (1995) Geochemical controls on the kinetics of quartz fracture at subcritical tensile stresses. *J Geophys Res Solid Earth* 100:22349–22359
- [15] Bai T, Pollard DD, Gao H (2000) Explanation for fracture spacing in layered materials. *Nature* 403:753–756
- [16] Ilgen AG, Heath JE, Akkutlu IY, Bryndzia LT, Cole DR, Kharaka YK, Kneafsey TJ, Milliken KL, Pyrak-Nolte LJ, Suarez-Rivera R (2017) Shales at all scales: exploring coupled processes in mudrocks. *Earth Sci Rev* 166:132–152
- [17] Mares VM, Kronenberg AK (1993) Experimental deformation of muscovite. *J Struct Geol* 15:1061–1075
- [18] Nesbitt HW, Young GM (1984) Prediction of some weathering trends of plutonic and volcanic rocks based on thermodynamic and kinetic considerations. *Geochim Cosmochim Acta* 48:1523–1534
- [19] Bailey DS (1984) Classification and structures of the micas. *Rev Miner Geochem* 13:1–12
- [20] Guggenheim S, Chang Y-H, Koster van Groos AF (1987) Muscovite dehydroxylation: high-temperature studies. *Am Miner* 72:537–550
- [21] Pant R, Hu L, Zhang G (2013) Anisotropy of mica probed by nanoindentation. In: Laloui L, Ferrari A (eds) *Multiphysical testing of soils and shales*. Springer, Berlin, p 239
- [22] Mann AB, Pethica JB (1996) Nanoindentation studies in a liquid environment. *Langmuir* 12:4583–4586
- [23] Oliver WC, Pharr GM (1992) An improved technique for determining hardness and elastic modulus using load and displacement sensing indentation experiments. *J Mater Res* 7:1564–1583
- [24] Oliver WC, Pharr GM (2004) Measurement of hardness and elastic modulus by instrumented indentation: advances in understanding and refinements to methodology. *J Mater Res* 19:3–20
- [25] Knauss KG, Wolery TJ (1989) Muscovite dissolution kinetics as a function of pH and time at 70 °C. *Geochim Cosmochim Acta* 53:1493–1501
- [26] Lucas BN, Oliver WC, Pharr GM, Loubet JL (1997) Time dependent deformation during indentation testing. *MRS Proc* 436:233–238
- [27] Gauthier M, Nourine M (2007) Capillary force disturbances on a partially submerged cylindrical micromanipulator. *IEEE Trans Rob* 23:600–604
- [28] Chen J, Bull SJ (2006) On the relationship between plastic zone radius and maximum depth during nanoindentation. *Surf Coat Technol* 201:4289–4293
- [29] Lawn BR, Cook RF (2012) Probing material properties with sharp indenters: a retrospective. *J Mater Sci* 47:1–22. <https://doi.org/10.1007/s10853-011-5865-1>
- [30] Zhang J, Hu L, Pant R, Yu Y, Wei Z, Zhang G (2013) Effects of interlayer interactions on the nanoindentation behavior and hardness of 2:1 phyllosilicates. *Appl Clay Sci* 80–81:267–280
- [31] Barsoum MW, Murugaiah A, Kalidindi SR, Zhen T (2004) Kinking nonlinear elastic solids, nanoindentations, and geology. *Phys Rev Lett* 92:255508
- [32] Basu S, Zhou A, Barsoum MW (2009) On spherical nanoindentations, kinking nonlinear elasticity of mica single crystals and their geological implications. *J Struct Geol* 31:791–801
- [33] Zhang G, Wei Z, Ferrell RE (2009) Elastic modulus and hardness of muscovite and rectorite determined by nanoindentation. *Appl Clay Sci* 43:271–281
- [34] Schuh CA, Mason JK, Lund AC (2005) Quantitative insight into dislocation nucleation from high-temperature nanoindentation experiments. *Nat Mater* 4:617–621
- [35] Dimiduk DM, Woodward C, LeSar R, Uchic MD (2006) Scale-free intermittent flow in crystal plasticity. *Science* 312:1188–1190
- [36] Csikor FF, Motz C, Weygand D, Zaiser M, Zapperi S (2007) Dislocation avalanches, strain bursts, and the problem of plastic forming at the micrometer scale. *Science* 318:251–254
- [37] Chakravarti IM, Laha RG, Roy J (1967) *Handbook of methods of applied statistics*, vol I. Wiley, New York, pp 392–394
- [38] Lawn BR, Evans AG, Marshall DB (1980) Elastic/plastic indentation damage in ceramics: the median/radial crack system. *J Am Ceram Soc* 63:574–581
- [39] Anstis GR, Chantikul P, Lawn BR, Marshall DB (1981) A critical evaluation of indentation techniques for measuring fracture toughness: I, direct crack measurements. *J Am Ceram Soc* 64:533–538
- [40] Cook RF (2020) A critical evaluation of indentation crack lengths in air. *J Am Ceram Soc* 103:2278–2295
- [41] Cook RF, Roach DH (1986) The effect of lateral crack growth on the strength of contact flaws in brittle materials. *J Mater Res* 1:589–600
- [42] Cook RF (2015) Multi-scale effects in the strength of ceramics. *J Am Ceram Soc* 98:2933–2947
- [43] Cook RF, Liniger EG, Pascucci MR (1994) Indentation fracture of polycrystalline cubic materials. *J Hard Mater* 5:190–212
- [44] Cook RF, Liniger EG (1993) Kinetics of indentation cracking in glass. *J Am Ceram Soc* 76:1096–1106
- [45] Shannon RD (1976) Revised effective ionic radii and systematic studies of interatomic distances in halides and chalcogenides. *Acta Cryst A* 32:751–767

- [46] Faulkner DR, Jackson CAL, Lunn RJ, Schlische RW, Shipton ZK, Wibberley CAJ, Withjack MO (2010) A review of recent developments concerning the structure, mechanics and fluid flow properties of fault zones. *J Struct Geol* 32:1557–1575
- [47] Bak P, Tang C, Wiesenfeld K (1987) Self-organized criticality: an explanation of  $1/f$  noise. *Phys Rev Lett* 59:381–384
- [48] Bak P, Tang C, Wiesenfeld K (1988) Self-organized criticality. *Phys Rev A* 38:364–374
- [49] Markovic D, Gros C (2014) Power laws and self-organized criticality in theory and nature. *Phys Rep* 536:41–74
- [50] Petri A, Paparo G, Vespignani A, Alippi A, Costantini M (1994) Experimental evidence for critical dynamics in microfracturing processes. *Phys Rev Lett* 73:3423–3426
- [51] Tewari S, Schiemann D, Durian DJ, Knobler CM, Langer SA, Liu AJ (1999) Statistics of shear-induced rearrangements in a two-dimensional model foam. *Phys Rev E* 60:4385–4396
- [52] Shimanek J, Rizzardi Q, Sparks G, Derlet PM, Maass R (2020) Scale-dependent pop-ins in nanoindentation and scale-free plastic fluctuations in microcompression. *J Mater Res* 35(2):196–205
- [53] Zohar YC, Yochelis S, Dahmen KA, Jung G, Paltiel Y (2013) Controlling avalanche criticality in 2D nano arrays. *Sci Rep* 3:1845
- [54] Sethna JP, Dahmen KA, Myers CR (2001) Crackling noise. *Nature* 410:242–250

**Publisher's Note** Springer Nature remains neutral with regard to jurisdictional claims in published maps and institutional affiliations.